Advanced Materials

ADVANCED MATERIALS
www.advmat.de

RESEARCH ARTICLE

A Dopamine Driven Dual-Amplifier Strategy for High Performance Bioorganic Piezoelectrics via Secondary-Structure Modulation and Synergistic Molecular Dipoles

Xin Tan[1] | He Wang[1] | Ruilu Zhou[1] | Haipeng Chen[1] | Huifen Ding[1] | Xiaoke Zhang[2] | Han Ouyang[3] | Tianyan Zhong[1] | Jinlin Song[1]

[1]College of Stomatology, Chongqing Key Laboratory of Oral Diseases, Chongqing Municipal Key Laboratory of Oral Biomedical Engineering of Higher Education, Chongqing Medical University, Chongqing, P. R. China | [2]Roentgen Laboratory, Shanghai, P. R. China | [3]School of Nanoscience and Engineering, School of Chemical Sciences, University of Chinese Academy of Sciences, Beijing, P. R. China

Correspondence: Tianyan Zhong (tianyanzhong@hospital.cqmu.edu.cn) | Jinlin Song (songjinlin@hospital.cqmu.edu.cn)

Received: 17 March 2026 | **Revised:** 11 June 2026 | **Accepted:** 1 July 2026

Keywords: biomaterials | digital healthcare | dopamine hydrochloride | piezoelectricity | silk fibroin

ABSTRACT

Bio-proteins with intrinsic piezoelectricity are highly promising for bioelectronics due to their tunable conformations, biocompatibility, and biodegradability. However, their practical applications are severely constrained by difficulties in regulating piezoelectric domains and inherent mechanical brittleness. In this study, we propose a small-molecule dual-amplifier strategy to achieve high performance piezoelectric biomaterials. By introducing a dopamine-mediated modulation approach, a silk fibroin-based film with an enhanced piezoelectric coefficient of up to 12.7 pC N^{-1} is obtained. This performance boost is attributed to a dual mechanism: the dopamine-induced promotion of β-sheet formation in silk fibroin, which strengthens its intrinsic piezoelectricity, and the synergistic contribution of piezoelectric dipole moments from dopamine. In addition, the film exhibits superior mechanical robustness and flexibility, tunable stability in aqueous environments, as well as excellent in vitro/vivo biocompatibility. When applied to the sensing of temporomandibular joint motion and oral occlusal contact patterns, the resulting sensors demonstrate high sensitivity and long-term stability. Furthermore, the generated voltage signals can be effectively encoded and converted into digital information, facilitating data processing and analysis. These results demonstrate small-molecule modulation represents a reliable approach for enhancing the piezoelectricity of structurally complex proteins, offering a simple and innovative pathway toward the development of high-performance bio-piezoelectric materials for digital healthcare.

1 | Introduction

Bio-piezoelectric materials have attracted considerable interest owing to their favorable biocompatibility, biodegradability and abundant availability [1, 2]. Most importantly, owing to their naturally diverse conformations, some biomaterials (e.g., amino acids, peptides, and proteins) exhibit high intrinsic piezoelectric potential [3, 4]. For instance, glycine has a predicted piezoelectric coefficient of up to 178 pm/V, while silk fibroin (SF) and some other biomolecules are also predicted to exhibit strong

Xin Tan and He Wang contributed equally to this work.

piezoelectric responses, highlighting their great potential for applications in biosensing [5–7]. However, the difficulties in controlling their molecular conformations and regulating the piezoelectric phase, often result in weak or unstable piezoelectric performance [8, 9]. In addition, inherent mechanical limitations—such as excessive brittleness, lack of elasticity, or insufficient mechanical strength—further hinder their implementation in biomedical applications [10, 11].

Among the various bio-piezoelectric materials investigated, SF has attracted particular attention in the biomedical field due to its controllable β-sheet content, piezoelectricity, mechanical performance and biodegradation rate, as well as favorable biocompatibility [12–15]. Nevertheless, practical applications of SF remain constrained by issues such as unstable piezoelectric performance, pronounced brittleness, and complex fabrication processes, which limit its broader implementation in bioelectronic applications [16–18]. Recently, small molecules have attracted growing interest for their role in modulating the structural configurations of biomaterials. Through various covalent or noncovalent interactions, these small molecules can induce ordered arrangements of crystalline phases or organic polymer chains, thereby influencing their functional properties [19, 20]. Among these molecules, mussel-inspired dopamine hydrochloride (DA) exhibits remarkable chemical versatility and broad interfacial affinity owing to its catechol groups [21–23]. This allows it to play a key role in promoting the formation and alignment of piezoelectric crystalline phases [24, 25], suggesting its potential utility in regulating the piezoelectric performance of biomaterials via conformational control.

This study proposes a dual-functional small-molecule strategy to regulate the piezoelectric properties of SF films (Scheme 1). By introducing DA to structurally regulate the SF matrix, a dual amplification of the piezoelectric effect is achieved. On the one hand, DA promotes the formation of β-sheet and enhances crystallinity, thereby optimizing and stabilizing the piezoelectric conformation of SF and significantly improving its piezoelectric performance. On the other hand, DA itself possesses a considerable dipole moment and intrinsic piezoelectricity. Under external stress, it synergistically responds with the dipoles of SF, leading to an enhanced overall piezoelectric responsiveness of the composite DA/SF film. Benefiting from this dual enhancement mechanism, the fabricated DA/SF film exhibits a piezoelectric coefficient (d_{33}) of up to 12.7 pC/N, surpassing that of most previously reported bio-piezoelectric films. Moreover, the introduction of DA improves the toughness of SF film by increasing both tensile strength and elongation at break. These mechanical adaptations make the film suitable for detecting subtle joint movements and withstanding cyclic loading. The DA/SF films demonstrate excellent sensitivity and stability in monitoring temporomandibular joint activity and occlusal contact patterns during mastication. The acquired waveform data can be converted and encoded into digital information, laying a solid foundation for its potential integration into intelligent healthcare systems. Finally, the film exhibits tunable stability in aqueous environments, along with favorable in vitro and in vivo biocompatibility, demonstrating its strong potential for applications in sustainable bioelectronics. Overall, this work provides a simple, effective, and environmentally friendly strategy for improving bio-piezoelectric films, which is expected to facilitate their future application in biosensing and implantable electronics.

2 | Results and Discussion

2.1 | Characterization of DA/SF Films

SF is a biomaterial possessing complex hierarchical structure, which mainly exists in two conformation types: silk I, composed mainly of random coils, α-helices, β-turns and side chains; and silk II, dominated by anti-parallel β-sheet nanocrystals stabilized via hydrogen bonding [26, 27]. Current research points out that piezoelectricity of SF is closely correlated with β-sheet crystallinity and crystalline orientation [28]. In addition, DA exhibits considerable potential in regulating the formation and alignment of piezoelectric phases [24]. Therefore, the incorporation of DA into SF films is expected to significantly influence their piezoelectric properties, motivating the synthesis of DF/SF composite films. Figure 1A illustrates fabrication process of DA/SF films. Regenerated SF (RSF) solutions were prepared according to the reported protocols [29], while DA was dissolved separately in Tris buffer. Then the DA solution and RSF solution were mixed in different ratios (0:10, 1:10, 2:10, 3:10, and 4:10, corresponding to PSF, 1DSF, 2DSF, 3DSF and 4DSF). The obtained homogeneous mixtures were cast on petri dishes, and films were formed through slow solvent evaporation at room temperature. This straightforward method does not require complex processing steps or advanced instruments, offering advantages in terms of time efficiency, environmental friendliness, and scalability for mass production.

As displayed in Figures 1B and S1, both PSF and 2DSF films show high optical transparency. The DA/SF films present a brown appearance due to the incorporation of DA. In the wavelength range of 400–800 nm, the UV–visible (vis) transmittance of PSF and DA/SF films is 75%–85% and 45%–65%, respectively, which is beneficial for observing underlying skin tissue states in biosensing applications. In addition, the DA/SF films exhibit excellent elasticity, flexibility, and deformability (Figure 1B). Tensile stress-strain tests (Figure 1C) demonstrate that the mechanical properties of DA/SF films vary with DA content. Specifically, as the DA concentration increases, the elongation at break initially increases and then decreases, while the tensile strength and Young's modulus display a fluctuating trend characterized by alternating decreases and increases. The 2DSF film exhibits the most balanced overall mechanical performance among all DA-containing groups. Compared with PSF films, this 2DSF film shows enhanced tensile strength and elongation at break, accompanied by a slightly reduced Young's modulus, indicating improved deformation compliance. Such mechanical adaptability is particularly beneficial for flexible sensing applications, which can realize conformal contact with skin or muscle tissues and effectively catch physiological deformations. It should be noted that the mechanical properties of the DA/SF films exhibited a non-monotonic dependence on DA concentration. This behavior may be attributed to the significant influence of DA concentration on the hydrogen-bonding interactions between SF and DA, as well as on the contact area between SF and polar solvents, thereby inducing conformational changes in SF and consequently affecting its mechanical properties (Figures S2–S5; Notes S1 and

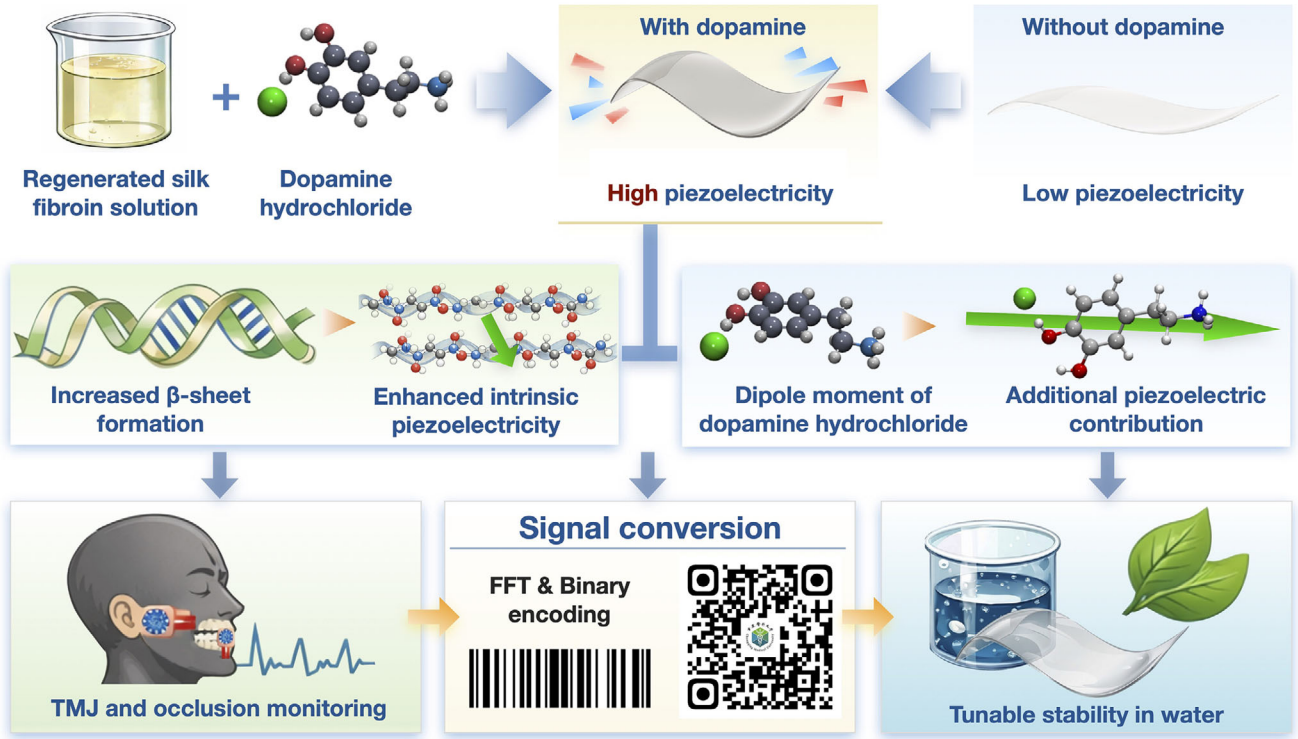

SCHEME 1 | Schematic illustration of the small-molecule dual-amplifier strategy for fabricating enhanced SF-based piezoelectrics.

S2). Furthermore, Atomic force microscope (AFM) indicates that the films present smooth and uniform surfaces, along with low nanoscale roughness (Figure 1D). Scanning electron microscopy (SEM) and energy-dispersive x-ray spectroscopy (EDS) analyses (Figure 1E) indicate that SF-based films possess uniform surface and cross sectional structures. In DA/SF films, chlorine elements which act as markers of DA are evenly spread on whole surface and cross section, thus confirming uniform incorporation of DA inside SF matrix.

As a protein-based film, the properties of DA/SF are closely related to its microstructure. Fourier-transform infrared (FTIR) spectra (Figures 1F and S6A) of the various SF films present that all samples exhibit a prominent absorption band in the amide I region (1600–1700 cm^{-1}), which originates from the C═O stretching vibration of amide groups, along with the amide II band at 1500–1600 cm^{-1} arising from N—H bending and C—N stretching vibrations, and the amide III band at 1200–1300 cm^{-1} associated with N–H bending vibrations [30]. With the incorporation of DA, detectable changes in intensity and peak shifts were observed in the amide I band (1620–1650 cm^{-1}), indicating significant structural alterations in the SF films. To further quantitatively analyze the secondary structure of all samples, the amide I bands were subjected to fourier self-deconvolution and second-derivative peak fitting (Figures 1G,H and S6B,C). Absorption peaks located at 1610–1635 cm^{-1} and 1690–1705 cm^{-1} correspond to β-sheet structures, those at 1635–1665 cm^{-1} are attributed to α-helices and random coils, and peaks at 1665–1690 cm^{-1} are assigned to β-turns [31]. Based on these assignments, statistical analysis reveals that the β-sheet content in 2DSF and 3DSF films (46% and 45%) increases markedly compared with PSF films (34%). In contrast, PSF and 1DSF films show higher percentages of α-helix and random coil structures (58% and 58%), while 4DSF films show an increased β-turn content (22%). The non-monotonic variation of SF secondary structure with DA concentration can be explained by concentration-dependent intermolecular interactions. MD simulations and differential FTIR spectral analysis showed that intermediate DA concentrations promote effective noncovalent interactions with SF, facilitating the formation of ordered and compact structures, consistent with the higher β-sheet content in the 2DSF and 3DSF groups (Figures S3 and S4; Figure 1G). At low DA concentrations, insufficient DA–SF interactions fail to induce ordered SF structures, resulting in lower β-sheet content in 1DSF (Figures S3 and S4; Figure 1G). In contrast, excessive DA promotes self-associated hydrogen bonding among DA molecules, reducing the effective interactions required for SF crosslinking and β-sheet formation, as reflected by the lower β-sheet content in 4DSF (Figures S3–S5 and 1G). These results support that an appropriate DA/SF ratio is essential for simultaneously optimizing SF structural organization and mechanical performance [19, 24].

The x-ray diffraction (XRD) patterns (Figure 1I) display that SF films of all groups present wide diffraction characteristics within the 2θ scope of 10°–20°, and a characteristic peak stand at 2θ = 20°–22°. Variations in peak width among different samples indicate differences in their crystalline structures. The crystallinity was further quantified via the integration of areas under the diffraction curves (Figure S7). The results (Figure 1J) indicate that with the increase of DA content, the crystallinity of the films initially increases and then decreases. The 2DSF film shows a moderate crystallinity (21.3%), which is still significantly higher than that of PSF (13.1%). Notably, crystallinity did not exhibit the same trend as β-sheet content. This discrepancy arises

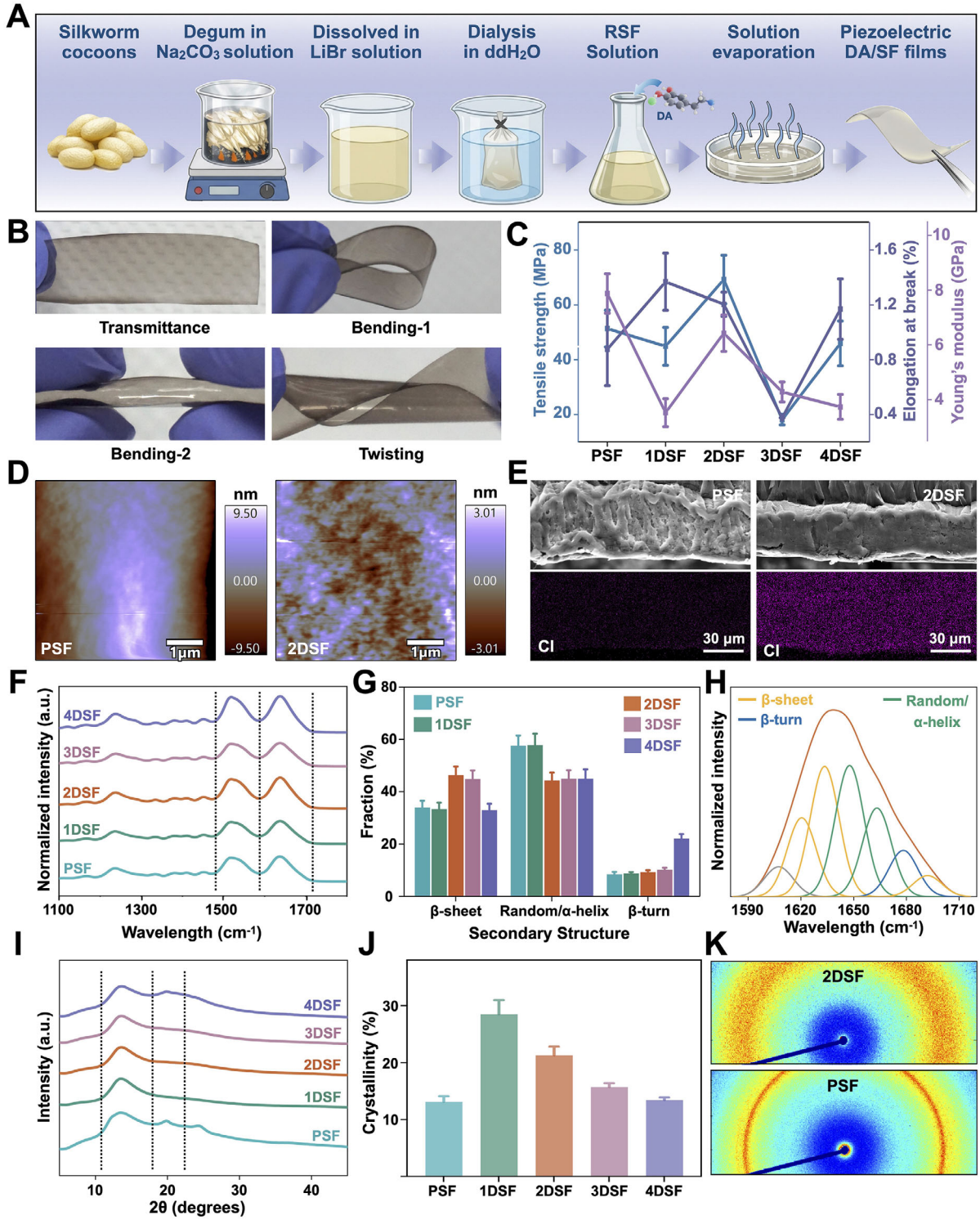

FIGURE 1 | Characterization of DA/SF films. (A) A schematic illustration depicts the fabrication procedure of DA/SF films. (B) Representative photographs demonstrate the transparency and flexibility of the DA/SF films. (C) Tensile strength, elongation at break, and Young's modulus of SF films incorporating different DA contents. DA solution: RSF solution = 0:10 (PSF), 1:10 (1DSF), 2:10 (2DSF), 3:10 (3DSF), and 4:10 (4DSF). (D) AFM images reveal the surface microtopography of PSF and 2DSF films. (E) Cross sectional SEM images (top) together with the corresponding EDS elemental mapping (bottom) illustrate the internal morphology of the SF films and the spatial distribution of Cl. (F) FTIR spectra collected in the range of 1100–1800 cm^{-1} display the characteristic amide I–III bands of different SF films. (G) The relative contents of secondary conformations in various SF films are summarized based on spectral deconvolution. (H) Detailed analysis of the amide I region in the FTIR spectra elucidates the secondary structural distribution of 2DSF, where β-sheet structures are identified at 1610–1635 cm^{-1} and 1690–1705 cm^{-1}, random coils and α-helices at 1635–1665 cm^{-1}, and β-turns at 1665–1690 cm^{-1}. (I–J) XRD patterns of different SF films, along with the corresponding quantitative crystallinity analysis, highlight the DA-dependent crystalline evolution. (K) WAXS results present the crystalline quality of PSF and 2DSF films.

because crystallinity depends not only on the β-sheet fraction but also on crystallite size, molecular packing regularity, and long-range structural ordering [26, 32–34]. As shown in Figure 1G,J, 1DSF exhibited higher crystallinity than PSF despite their similar β-sheet contents, which may be attributed to its larger crystallite size (Figure S8). In addition, wide-angle x-ray scattering (WAXS) results demonstrate that the crystalline quality of PSF films was superior than that of 2DSF films (Figure 1K). These results indicate that DA incorporation causes notable changes to the β-sheet content and crystallinity of SF. These structural modifications are probably the key factors that control the observed changes in macroscopic properties of the films.

2.2 | Piezoelectric Performance of DA/SF Films

The macroscopic ferroelectric behavior was evaluated by measuring the polarization–electric (P–E) field hysteresis loops of SF films with different DA concentrations. As Figure 2A illustrates, 2DSF film exhibits pronounced polarization and superior ferroelectric characteristics, which is closely related to the well-aligned orientation of piezoelectric domains inside the film, thereby confirming its favorable piezoelectric behavior. The dielectric property test (Figures 2B and S9) indicates that the PSF, 1DSF and 2DSF films exhibit relatively low dielectric constants (<4.5) and dielectric loss, which is beneficial for achieving higher piezoelectric voltage output [35]. In contrast, the dielectric constants (>6) and dielectric loss of the 3DSF and 4DSF films increase markedly, which may adversely affect the voltage output performance of the films [36]. Quasistatic d_{33} measurements (Figures 2C and S10–S14) further reveal that the d_{33} of the films initially increases and then decreases with increasing DA content, and Notably, the 2DSF film achieves a maximum d_{33} value of 12.7 pC N^{-1}, surpassing those of most previously reported biopiezoelectric films, including γ-glycine/PVA (10.4 pC N^{-1}) [37], silk nanoribbons (7.7 pm V^{-1}) [11], β-glycine/PDMS (5.7 pC N^{-1}) [24], and DL-alanine/PDMS (4.8 pC N^{-1}) [38]. Relative to recently reported piezoelectric SF-based materials, the DA/SF films developed in this study offer a compelling combination of high piezoelectric output, facile fabrication, and reduced time and energy requirements, highlighting their potential for scalable and sustainable applications [7, 9, 11, 14, 30, 39] (Table S1). In addition, although commonly used methanol or ethanol treatments can promote β-sheet formation, they significantly increase the brittleness of SF films without markedly improving their piezoelectric performance (Figures S15–S18). In contrast, DA incorporation enhances SF piezoelectricity while better preserving film flexibility. Furthermore, temperature-dependent stability tests showed that the DA/SF films maintained a d_{33} value above 12.3 pC/N within the physiological temperature range of 20°C–40°C (Figure S19). Even at an elevated temperature of 70°C, the d_{33} value remained higher than 6 pC/N, indicating that the DA/SF films retain considerable piezoelectricity under both physiological and relatively harsh thermal conditions [40, 41]. These results provide compelling evidence for the effectiveness of DA incorporation in enhancing the piezoelectric performance of SF films.

The microscopic piezoelectric performance of the samples was investigated using piezoresponse force microscopy (PFM). Figure 2D–I presents the PFM out-of-plane (OOP) amplitude mappings, PFM-OOP phase mappings, and the corresponding quantitative phase distributions of the PSF, 2DSF, and 3DSF films, respectively. Specifically, the three-dimensional (3D) PFM-OOP amplitude morphology of the PSF film exhibits a dispersed and highly nonuniform piezoelectric response (Figure 2D). The corresponding PFM-OOP phase mapping and phase histogram (Figure 2G) reveal a heterogeneous phase distribution with pronounced opposing phases, indicating inconsistent piezoelectric domain alignment directions within the film. Such disordered domain orientations may lead to mutual cancellation of piezoelectric vectors along different directions, thereby weakening the overall OOP piezoelectric performance of the film [42–44]. In contrast, the 2DSF and 3DSF films display relatively uniform piezoelectric responses in their 3D PFM-OOP amplitude morphologies (Figure 2E,F). Moreover, the PFM-OOP phase mappings and phase histograms (Figure 2H,I) show homogeneous phase distributions with minimal phase opposition, suggesting a high degree of consistency in local piezoelectric domain alignment.

Furthermore, ferroelectric hysteresis loop measurements were carried out. For the PSF film, no characteristic butterfly-shaped amplitude loops were observed (Figure 2J), indicating its weak ferroelectric behavior. In contrast, the 2DSF films exhibit well-defined butterfly-shaped amplitude loops accompanied by an approximately 180° phase shift at the point of minimum amplitude, demonstrating pronounced ferroelectricity (Figure 2K). Furthermore, analysis of the PFM data yielded an inverse piezoelectric coefficient of up to 35 pm/V for the 2DSF films. Although the amplitude loops of the 3DSF films are less distinct and characteristic than those of the 2DSF films, they still indicate evident ferroelectric behavior (Figure 2L). By integrating both macroscopic and microscopic characterization results, the 2DSF films are identified as exhibiting the most superior ferroelectric and piezoelectric properties. These findings further validate the feasibility of employing small molecules such as DA to enhance the piezoelectricity of biomaterials with complex hierarchical structures.

2.3 | Mechanism of DA on SF Biofilm Piezoelectric Performance

Based on the widely accepted polar stacking of antiparallel β-sheets in SF [26, 45], molecular models of polypeptide double chains with four distinct relative configurations (antiparallel, close approach, register shift 1, and register shift 2) were constructed (Figure S20), and calculations based on density functional theory (DFT) were subsequently performed. As Figure 3A–D shows, negative charges are strongly constructed around the O and N atoms due to their high electronegativity. This leads to dense charge density contour lines, which are an indication that electron density decays rapidly from atomic centers to surrounding regions. On the contrary, the C and H atoms in the hydrocarbon backbone have lower electronegativity, which causes more delocalized electron clouds and sparser contour lines. This situation shows a more gradual change in electron density. Therefore, when polypeptide chains take an antiparallel configuration, charge density is mainly gathered around the N atoms and O atoms at the edges of the two chains (Figure 3A). One end of each chain shows a slightly higher charge density than the

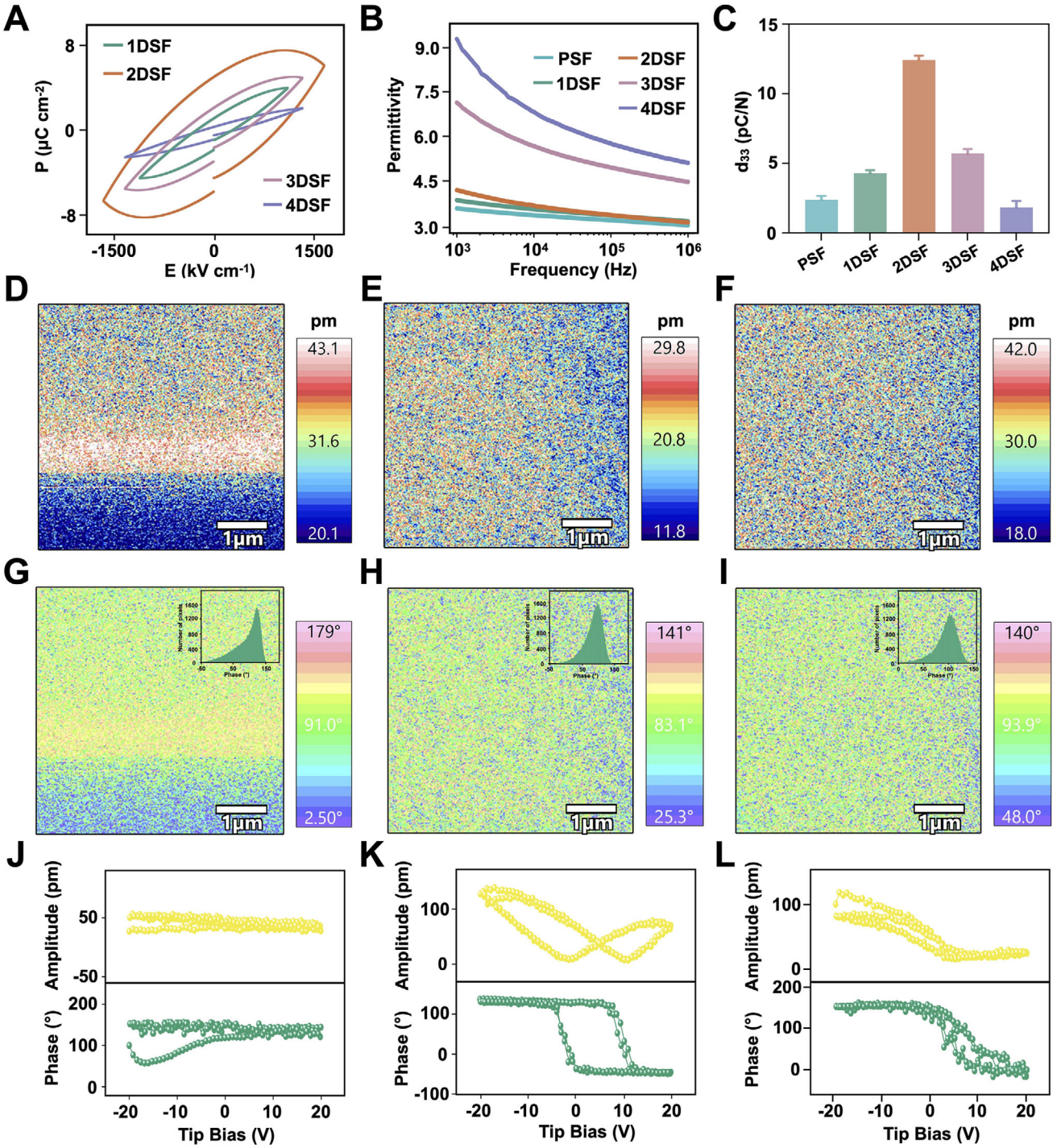

FIGURE 2 | Piezoelectric performance of DA/SF films. (A) P–E hysteresis loops reveal the ferroelectric characteristics of different SF films. (B) Relative permittivity of the SF-based films. (C) Results of the d_{33} measurement of various SF films. (D–L) PFM results illustrate nanoscale electromechanical responses across the SF films, including OOP amplitude maps (D–F), OOP phase maps (G–I), corresponding phase histograms (the inset at the upper-right corner of the phase maps), and ferroelectric hysteresis loops (J–L) for PSF films (D, G, J), 2DSF films (E, H, K), and 3DSF films (F, I, L).

other end, and weak interchain interaction exists. This structural asymmetry and nonuniform charge density distribution finally cause a net dipole moment (4.61 D) for the two-chain system along the *Y* axis, with a deviation angle of 27.74° (Figure 3E). When the two polypeptide chains move close to each other, charge density of one chain becomes mainly distributed along the extended backbone, while that of the other chain is mainly localized at terminal regions (Figure 3B). At the same time, interchain interaction is strengthened. This may increase the overall symmetry of the charge density distribution of the two-chain system, thus partially compensating for the asymmetry that comes from individual chains. Hence, the system forms a

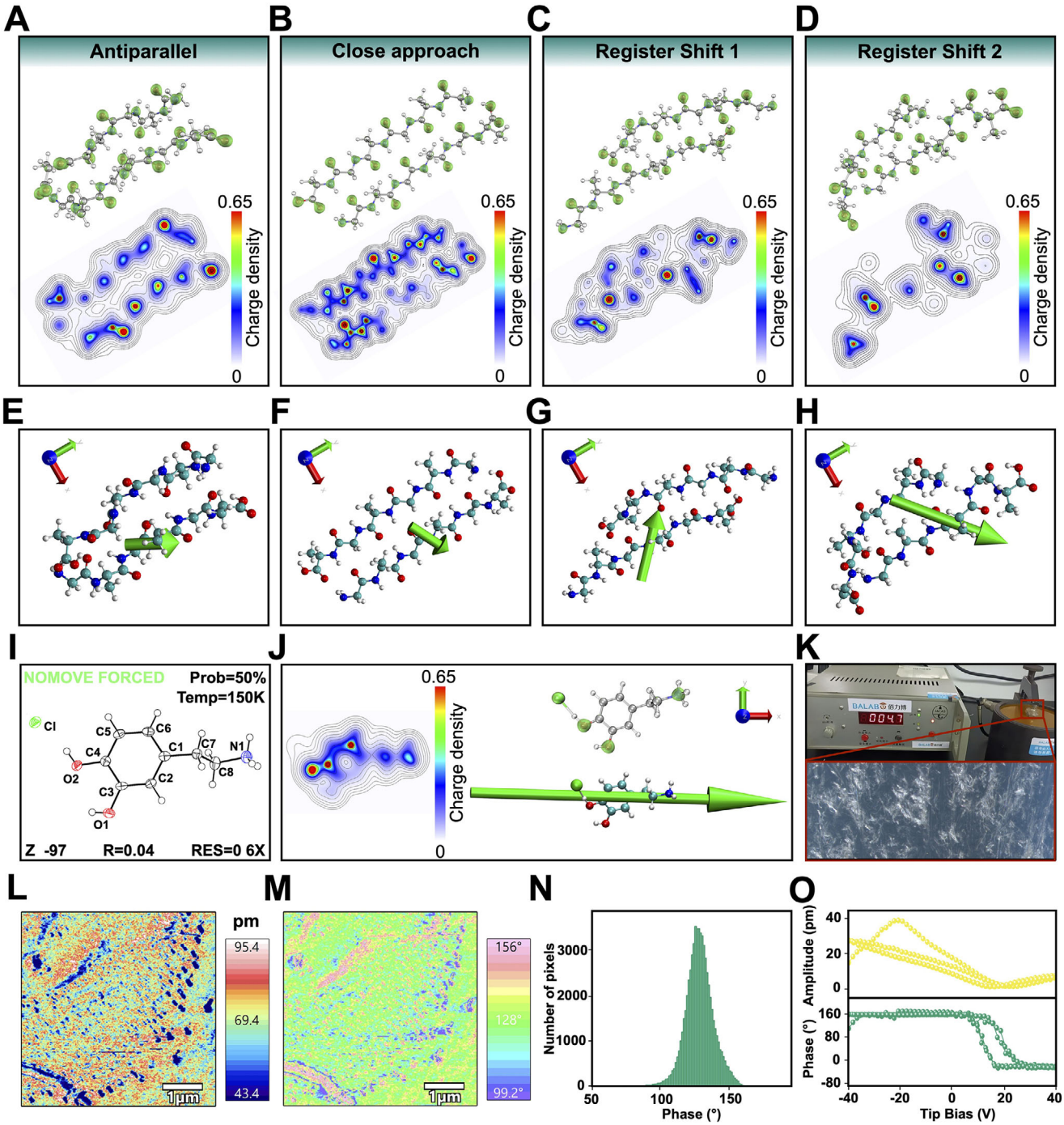

FIGURE 3 | Mechanism of DA in enhancing the piezoelectric performance of SF bio-films. (A–D) Four molecular models were constructed based on the anti-parallel arrangement of repetitive polypeptide chains in the β-sheet structure of SF. The charge density distribution (upper panels) and contour plots of charge density (lower panels) for each model are presented. (E–H) Computed molecular dipoles (green arrows) of the four models, including the antiparallel (E), close approach (F), register shift 1 (G), and register shift 2 (H). (I) Molecular structure of the acquired DA single crystal. (J) Contour plots of charge density (left), charge density distribution (upper right), and calculated dipoles (lower right) for DA. (K) The d_{33} measurement of DA/PDMS film (upper panel), and the magnified view of the surface morphology (lower panel). (L–O) PFM detection of the DA/PDMS film. The results include OOP amplitude mapping (L), OOP phase mapping (M), phase histogram (N), and ferroelectric hysteresis loop (O) for the film.

dipole moment (4.83 D) which is slightly larger than that of the antiparallel configuration, oriented along the *X* axis with a deviation angle of 26.85° (Figure 3F).

When longitudinal relative slippage takes place between the two antiparallel chains, great changes of electron cloud distribution can be observed. In slip configuration 1 (register shift 1), spatial separation between amido groups on the two antiparallel chains becomes larger, thereby exacerbating the nonuniformity of the charge density distribution (Figure 3C). Moreover, because amido groups at the chain edges are inherently oriented at a certain angle, the increased slip distance amplifies the overall structural

asymmetry of the two-chain system. Consequently, the net dipole moment is significantly enhanced, reaching 7.60 D and oriented along the *X* axis with a deviation angle of 43.72° (Figure 3G). In slip configuration II (register shift 2), both the distance and angular mismatch between the amido groups on the antiparallel chains increase, leading to further asymmetry in charge density distribution (Figure 3D). Under this configuration, the system generates a dipole moment of 11.29 D along the *X* axis with a deviation angle of 39.33°, representing the largest dipole moment among all the considered configurations (Figure 3H).

The above results indicate that the repetitive polypeptide sequences within the β-sheet structures of SF exhibit asymmetric structures and non-zero dipole moments at multiple relative positions, which may constitute an important origin of the intrinsic piezoelectricity of SF. According to previous research, the piezoelectric performance of SF is related to the β-sheet crystallinity and crystalline orientation [28, 30]. The former reflects the fraction of structures in SF that can contribute dipole moments to the macroscopic piezoelectric response, while the latter determines whether these non-zero dipole moments can be aligned and superimposed in the same direction rather than oriented randomly and mutually canceled [5, 28, 46, 47]. Therefore, simply increasing the β-sheet content without considering crystalline orientation does not lead to a significant improvement in the piezoelectricity of SF. As shown in Figure 1G,J, the incorporation of DA increases the β-sheet content in SF; however, Figure 1K demonstrates that DA does not improve the orientation of the crystalline domains in SF. Accordingly, we speculate that the enhancement of the piezoelectric performance of SF arises from additional factors, particularly the intrinsic piezoelectricity of DA itself. Therefore, theoretical and experimental investigations were further conducted to verify the piezoelectric properties of DA.

Specifically, commercially available DA crystals were dissolved in tris buffer solutions (pH = 9.5) and recrystallized on the PDMS substrate via a slow evaporation process. Single crystals of DA were then selected for structural determination, revealing the molecular structure of DA under these conditions (FigureS 3I and S21–S23; Tables S2–S5). Results of DFT calculations (Figure 3J) show that the charge density of DA is mainly concentrated on two C atoms of the benzene ring and on the Cl atom near the ring, with an additional obvious charge density around the N atom. This pronounced structural asymmetry results in a substantial dipole moment of up to 30.31 D along the *X* axis (deviation angle: 1.64°), theoretically confirming its strong potential for piezoelectricity.

To further validate the theoretical predictions, the DA/PDMS films were prepared for subsequent characterization (Figure S24). The d_{33} of the composite film was measured, and a value as high as 4.7 pC/N was revealed (Figures 3K and S25), which exceeds that of some reported biomaterials [48–51]. The microscopic piezoelectric response of the crystal film was determined by PFM. The PFM-OOP amplitude mapping demonstrates a relatively uniform piezoelectric response across the film surface (Figure 3L). Moreover, the PFM-OOP phase mapping and corresponding phase histogram confirm a uniform phase distribution with minimal phase opposition, which suggests that the local piezoelectric domains have a consistent polarization orientation (Figure 3M,N). Furthermore, ferroelectric hysteresis loop measurements were conducted, and the existence of characteristic butterfly-shaped amplitude loops together with an approximately 180° phase shift at the minimum amplitude point indicates that DA/PDMS films exhibit pronounced ferroelectric behavior (Figure 3O). Collectively, these results prove that DA indeed exhibits distinct OOP piezoelectricity, which can be ascribed to its asymmetric molecular structure and nonuniform charge density distribution.

Considering that DA can self-polymerize into polydopamine (PDA), UV–vis characterization and control experiments were performed to confirm that the observed piezoelectric enhancement mainly originated from DA. The UV–vis spectra showed no characteristic broad absorption of PDA (Figure S26), indicating that significant DA self-polymerization did not occur under our preparation conditions. Furthermore, PDA-containing SF films were intentionally prepared (Note S3). Optical microscopy revealed that PDA formed pronounced local aggregates with a heterogeneous distribution within the SF matrix (Figure S27). DFT calculations showed that representative PDA structures possess significantly lower dipole moments than DA (Figure S28), and such disordered aggregation may further cause partial dipole cancellation [5, 52]. Consistently, PDA/SF films exhibited lower and more heterogeneous d_{33} values than DA/SF films (Figure S29). These results strongly support that the enhanced piezoelectricity observed in DA/SF films is mainly derived from DA rather than PDA.

In this research, DA plays a dual role in enhancing the piezoelectric property of SF-based films. On the one hand, DA induces the formation of a higher proportion of β-sheet structures within SF, which facilitates the constructive alignment and superposition of dipole moments in SF, thereby enhancing its inherent piezoelectric response. On the other hand, owing to its asymmetric molecular structure, DA itself contributes additional dipole moments to the composite film, further promoting the overall piezoelectric enhancement of the system. To our knowledge, this work is the first research that confirms the piezoelectric behavior of DA and makes use of this effect to improve the piezoelectric performance of biomaterials. It offers both theoretical insight and a technical reference for future efforts aimed at improving the piezoelectricity of biomaterials using small molecules.

2.4 | Output Performance of DA/SF-Based Piezoelectric Biosensor

To evaluate the voltage output performance of DA/SF film, it was made into a mechanical force sensor, in which the central layer consists of two 2DSF films connected in series, and the basic assembly structure is shown in Figure 4A. To investigate the operational stability of the biosensor, the pressure device was subjected to repeated cyclic loading and unloading. Figure 4B shows that the output voltage exhibited negligible fluctuation over 3000 consecutive cycles, demonstrating the strong mechanical reliability and long-term durability of the sensor. Moreover, the generated voltage shows a force-dependent increase, which highlights the outstanding electromechanical energy conversion ability of the DA/SF films (Figure 4C). Additionally, within the pressure range of 10–100 N, a clear linear correlation between the output voltage and applied pressure was established, which obtains a voltage sensitivity as high as 0.065 V/N (Figure 4D).

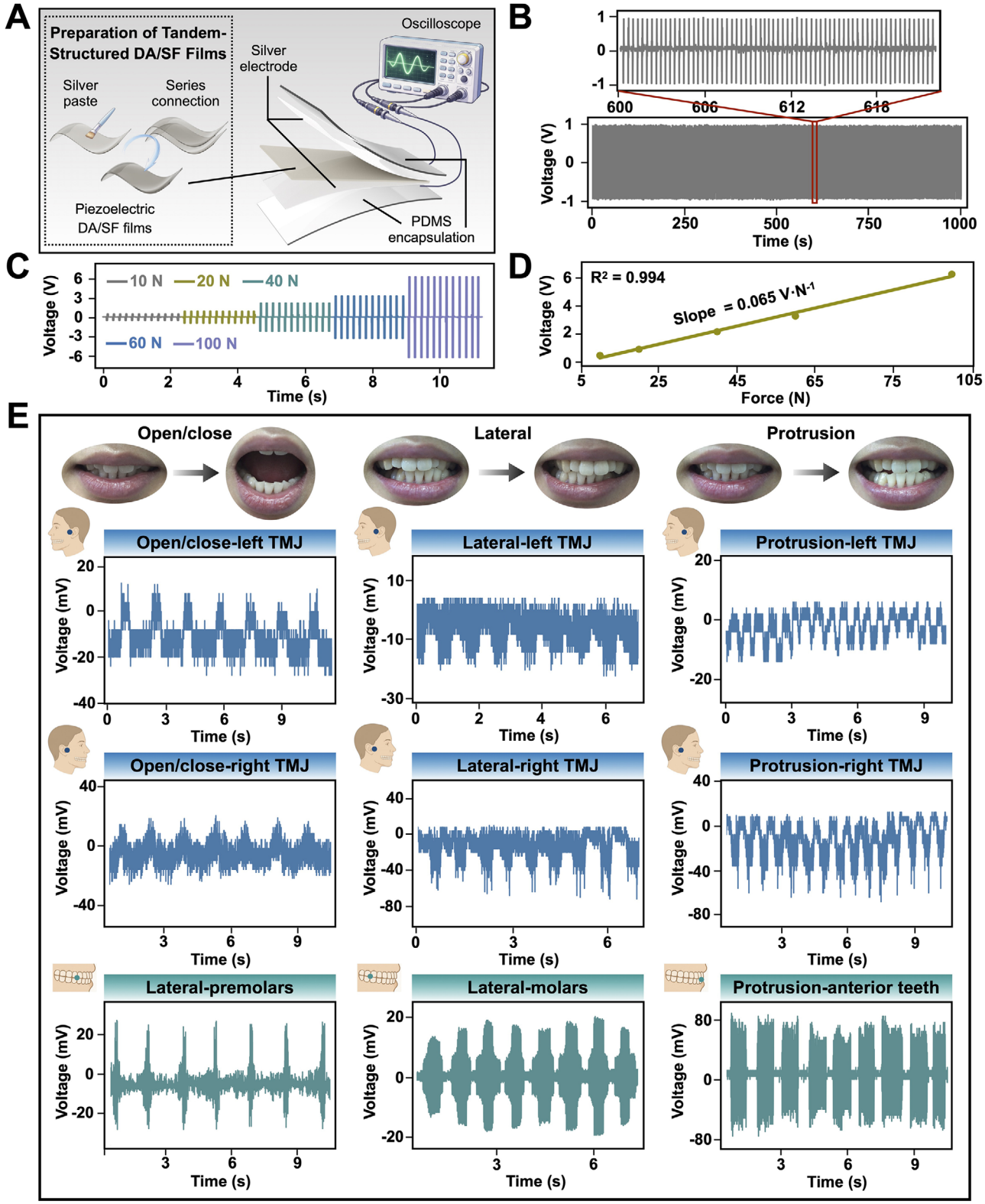

FIGURE 4 | Output performance of DA/SF-based piezoelectric biosensors. (A) Schematic illustration of the fabrication of DA/SF-based piezoelectric force sensors. (B) Long-term operational stability of the DA/SF film under repetitive mechanical loading (20 N, 3 Hz, 3000 cycles). (C) Force-dependent piezoelectric voltage responses of the device under progressively increased external loads. (D) Voltage-force linear fitting curve. (E) During mandibular opening–closing, lateral and protrusive movements, and distinct voltage waveforms were recorded from sensors positioned on the surfaces of the left and right TMJs, as well as from the occlusal surfaces of different tooth positions.

Given the superior piezoelectric sensing capability and favorable mechanical properties of the DA/SF film, it is expected to be suitable for monitoring complex physiological activities. Mastication is a fundamental process in dentate organisms, which not only has key function in food intake but also in keeping temporomandibular joint (TMJ) health [53]. Therefore, monitoring TMJ motion patterns and occlusal contact behaviors during mastication holds considerable diagnostic and therapeutic value for stomatognathic diseases [54, 55]. However, current devices have availability limitation and often depend on costly consumables or complicated instruments [56–58]. Moreover, during mastication, the surface deformation of TMJ is considerably smaller than that of larger joints like knee or elbow [55]. This necessitates the use of sensing films with high sensitivity to accurately capture the subtle surface deformations. In addition, contact patterns between maxillary and mandibular teeth are highly complex, and the irregular morphology of the occlusal surfaces results in non-uniform force distribution on the sensing film [59, 60]. Hence, this requires the sensing film to have enough mechanical strength and toughness to prevent early damage in monitoring process and to guarantee reliable sensing performance.

Therefore, the force sensor was attached to the surface of TMJ or to the occlusal surfaces of teeth to record voltage waveforms produced during several common mandibular movements associated with mastication. The results indicate that the device can sensitively capture detailed features of masticatory activities (Figure 4E). Specifically, during mandibular opening-closing movements, alternative upward and downward voltage peaks were observed at both the left and right TMJs, with downward peaks exhibiting greater widths than upward peaks. During lateral movements, continuous downward voltage peaks were detected at both TMJs, which may be attributed to the relatively large lateral forces generated at TMJs during such movements. When mandible performed protrusive movements, alternative upward and downward peaks were observed again at both TMJs, with downward peaks presenting higher amplitudes than upward peaks. Specifically, differences in waveforms between the left and right joints are probably related to asymmetries in joint morphology and the nonidentical force distributions experienced by each side. Additionally, distinct waveforms were recorded at the occlusal surfaces under different masticatory motions. During lateral movements, narrow and sharp bidirectional peaks were observed at the premolar region, whereas broader and blunter bidirectional peaks were detected at the molar region. These differences are likely associated with variations in occlusal surface morphology and force distribution between the two sites. During protrusive movements, incisal edges of mandibular anterior teeth mainly slide along the lingual surfaces of maxillary anterior teeth. Thus, regular rectangular-shaped voltage waveforms were recorded at corresponding occlusal sites. These findings validate the feasibility of using DA to improve the piezoelectricity of biomaterials with complex hierarchical structures, hence expanding their applications in biosensing field.

2.5 | Digital Processing of Information Collected by DA/SF Films-Based Sensors

The waveform signals generated by joint movements were then converted into digital information, which facilitates the centralized management and large-scale analysis of clinical datasets in future applications. First, fourier transformation was applied to voltage waveforms recorded by the sensor to get corresponding frequency spectrum [61]. Spectral analysis (Figure 5A) found that joint movement frequencies of volunteers were generally below 5 Hz, and dominant activity was concentrated in 0–2 Hz range. The output voltage varied between 0 and 16 mV, depending on the specific joint movement pattern and measurement location. Therefore, a binary encoding strategy was put forward to convert spectral information into digital data that is more convenient for storage and access. Specifically, five frequency bands (0–1, 1–2, 2–3, 3–4, and 4–5 Hz) were defined, and one threshold voltage was assigned to each band. Signal components over corresponding threshold were encoded as "1", and those below threshold were encoded as "0". By this way, spectral information related to each type of joint movement could be represented as one unique binary code (Figure 5B). Hence, encoding results were as follows: left TMJ open/close movement was encoded as "10000"; right TMJ open/close as "11000"; left TMJ lateral movement as "11010"; right TMJ lateral movement as "10010"; left TMJ protrusive movement as "01000"; right TMJ protrusive movement as "00000". These binary codes can be further converted into barcodes or visual QR codes that are recognizable by smartphones [62] (Figure 5C,D), enabling direct access to the corresponding joint movement waveform data and associated descriptive information. These results demonstrate the effective digitalization of TMJ activity signals acquired by the DA/SF film-based sensors, highlighting the potential of piezoelectric biomaterials for future applications in digital diagnostic and therapeutic technologies.

2.6 | Biocompatibility of DA/SF Films

As a natural protein derived from silkworm silk, SF possesses inherent and tunable biodegradability [63–65]. In addition, DA is a mussel-inspired small molecule with intrinsic biodegradability [66, 67]. Therefore, the DA/SF composite films are expected to exhibit biodegradable behavior. In this study, the solubility of DA/SF films was first investigated. As shown in Figure 6A, films that were not subjected to conventional crosslinking treatments (such as methanol immersion [14, 68]) were almost completely dissolved in phosphate-buffered saline (PBS) within 7 days. However, after immersion in ethanol for 1 h, the DA/SF films remained structurally stable in PBS for more than 1 week without noticeable dissolution or disintegration. Furthermore, the crosslinked films were dried after water immersion and their voltage output was evaluated, revealing no significant attenuation compared with films that had not been exposed to methanol and PBS (Figure S30). These results demonstrate the tunable stability of DA/SF films in aqueous environments, thereby broadening their potential applications in implantable and sustainable electronics.

The uncross-linked SF and DA/SF films were dissolved in PBS, and the obtained solutions were then added to the culture medium of bone marrow mesenchymal stem cells (BMSCs) to evaluate their in vitro biocompatibility. The CCK-8 assay results (Figure S31) show that, compared with the control group, the cells which are cultured with extracts from SF and DA/SF groups have proliferation rates at comparable levels. Live/dead cell staining (Figure 6B) discovers that, relative to the control group, neither SF group nor DA/SF group has a visible increasing number of dead

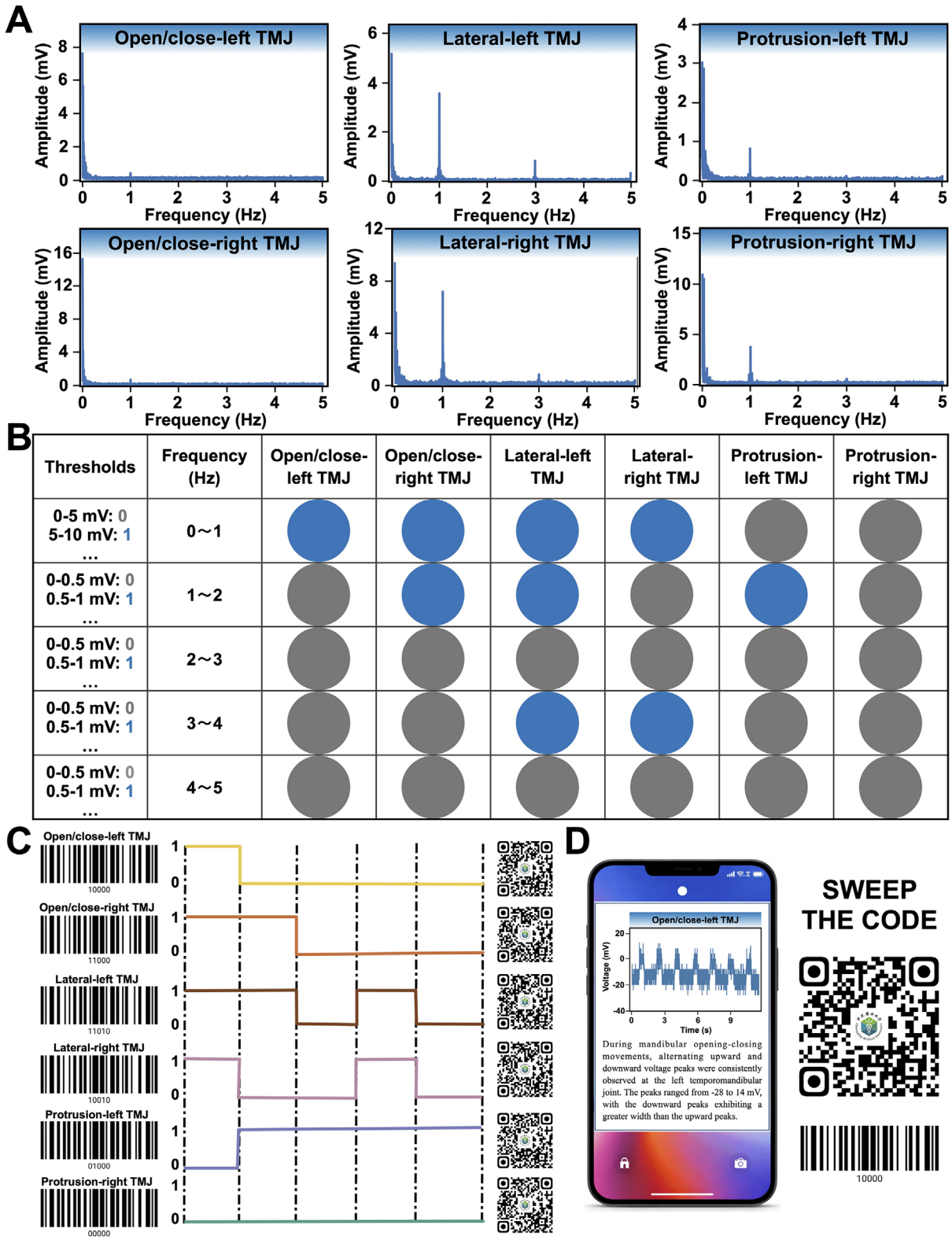

FIGURE 5 | Digital processing of information collected by DA/SF film-based sensors. (A) Frequency spectra of voltage signals collected from the surfaces of TMJs during various movements. (B) Binary encoding of the frequency-spectrum data for each group: within the 0–1 Hz band, voltages < 5 mV were encoded as "0", whereas voltages ≥ 5 mV were encoded as "1". Within the 1–2, 2–3, 3–4, and 4–5 Hz bands, voltages < 0.5 mV were encoded as "0", whereas voltages ≥ 0.5 mV were encoded as "1". (C) Barcodes and QR codes generated based on the binary-encoded data. (D) The generated barcodes and QR codes can be recognized by smartphones.

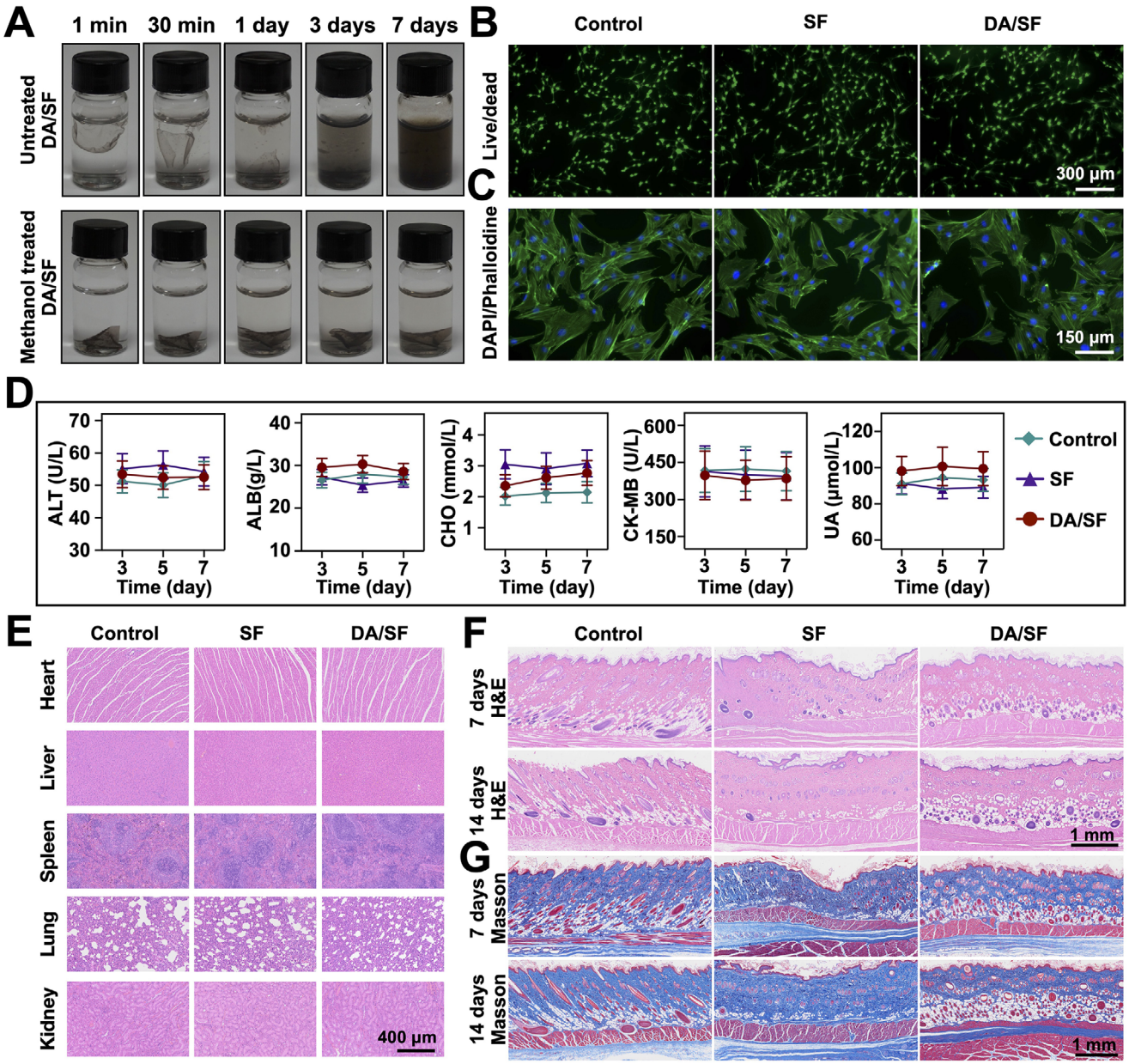

FIGURE 6 | Biocompatibility of DA/SF films. (A) Assessment of the solubility behavior of DA/SF (2DSF) films in PBS. (B) Proliferation of BMSCs, quantified by the CCK-8 assay after incubation with SF and DA/SF (2DSF) solutions at a concentration of 10 μg/mL. (C) Representative fluorescence micrographs obtained from viability assays, including live/dead staining in which viable and nonviable cells are visualized in green and red, respectively, as well as phalloidin/DAPI staining to highlight the cytoskeletal filamentous actin (green) and cell nuclei (blue). (D) Serum biochemical parameters measured in SD rats to evaluate systemic biological responses. (E) Histological sections of major organs collected from treated rats 7 days following implantation, visualized by H&E staining. (F, G) H&E and Masson's trichrome–stained histopathological images of skin tissue overlying unencapsulated SF and DA/SF (2DSF) films at 7 and 14 days after implantation, illustrating tissue architecture and collagen deposition.

cells. Cytoskeletal staining (Figure 6C) proves that BMSCs in all three groups present well-spread shapes, which indicates that the cellular states are good. Overall, these results confirm that both SF and DA/SF films have excellent in vitro biocompatibility.

The in vivo biocompatibility and degradation of SF and DA/SF films was further assessed via subcutaneous implantation operation in rat animals (Figure S32). Blood biochemical analyses (Figure 6D) demonstrate that, at 7 days post implantation, plasma parameters—including albumin (ALB), urea (UA), cholesterol (CHO), alanine aminotransferase (ALT), and creatine kinase-MB (CK-MB)—are kept inside normal value ranges. Histological analysis toward major organs discovers no obvious pathological changes or harmful tissue reactions (Figure 6E). Then, the soft tissues around the implantation positions were further examined. Histological evaluations which are based on hematoxylin and eosin (H&E) and Masson's trichrome staining (Figure 6F,G) found that both SF and DA/SF films disappeared within 7–14 days after implantation. Importantly, no visible structural damage was seen in the nearby skin or under-layer muscle tissues. The subcutaneous areas showed tissue structures that can be compared to those of control samples, and there is no existence

of infection, abscess formation or tumor growth at implantation sites, thus confirming the good in vivo biocompatibility and degradation of the implanted materials.

3 | Conclusions

This study proposes a small-molecule dual-amplifier strategy for achieving high performance bioorganic piezoelectric materials. By introducing DA to structurally modulate the SF matrix and forming composite films, the resulting films exhibit markedly enhanced piezoelecity, with a d_{33} reaching 12.7 pC/N, surpassing most previously reported bio-piezoelectric films. This enhancement arises from a synergistic mechanism: DA induces increased β-sheet formation in SF, thereby strengthening its intrinsic piezoelectricity, while its inherent molecular dipole moment provides an additional piezoelectric contribution. The DA/SF films also demonstrate excellent flexibility and mechanical robustness, enabling reliable sensing of subtle joint motions and withstanding of cyclic loading. Piezoelectric force sensors fabricated from these films show high sensitivity and stability in monitoring TMJ motion and occlusal contact patterns. Importantly, the acquired signals can be efficiently encoded and converted into digital information, facilitating clinical data organization, storage, and analysis, and highlighting their potential integration into digital diagnostic systems. Moreover, the DA/SF films exhibit tunable stability in aqueous environments, and favorable in vitro/vivo biocompatibility, underscoring their promise as implantable bio-piezoelectric materials. Overall, this work validates the effectiveness of using small-molecule DA to enhance the piezoelectric performance of structurally complex proteins, offering a simple yet powerful strategy for the development of next-generation high-performance bio-piezoelectric materials.

4 | Experimental Section

4.1 | Materials

Silkworm cocoons from *Bombyx mori* (*B. mori*) were purchased from an online store on Taobao (Hangzhou, China). Na_2CO_3 and LiBr were purchased from Macklin (Shanghai, China). Dialysis membranes(MD: 34 mm, MWCO 3.5 kD), and the phalloidine/DAPI were purchased from Solarbio (Beijing, China). Dopamine hydrochloride (DA, ≥98%, AR) was obtained from Aladdin (Shanghai, China). Tris-(hydroxymethyl)-aminoethane (≥98%, AR), along with the CCK-8 and calcein-AM/PI reagent kit from Beyotime (Shanghai, China).

4.2 | Preparation of RSF Solutions

RSF solution was prepared following previously published methods [29]. Briefly, silkworm cocoons were first sectioned into pieces of approximately 1 cm^2 and subjected to boiling in 0.02 M Na_2CO_3 for 30 min to eliminate sericin. Following the degumming process, the silk was rinsed with ddH_2O at least 3 times, manually pressed to remove excess water, and air-dried in a fume hood. The resulting dry silk was subsequently dissolved in 9.3 M LiBr and stirred at 60°C for 4 h until a homogeneous amber solution formed. The SF–LiBr solution was dialyzed against ddH_2O for 3 days using tubing with 3.5 kDa molecular weight cutoff. After dialysis, the solution was centrifuged at 9000 rpm and 4°C for 20 min to remove insoluble parts. The transparent supernatant collected from this step was taken as RSF and kept at 4°C. Therefore, mechanical shaking was kept as small as possible during all the process thus to avoid structure changes caused by force.

4.3 | Preparation of DA/SF Films

DA was dissolved into Tris buffer (pH 9.5) for making a stock solution at the concentration of 10 mg/mL. Therefore, the newly prepared DA solution was added into RSF solution according to volume ratios of 0:10, 1:10, 2:10, 3:10, and 4:10 separately. Gentle mixing of the two solutions was carried out, and the resulting mixture was moved into petri dishes using a pipette. 1.5 mL of the solution was spread to cover a 1 cm × 4 cm rectangular region. Then the solution was subjected to air-drying under ambient conditions so that a film could be formed. No additional poling treatment was applied to the DA/SF films prior to characterization

4.4 | Preparation of DA Crystals and DA/PDMS Films

DA solution was made according to methods stated before. The solution was moved onto PDMS films by pipette and spread to cover one 1 cm × 1 cm rectangular region per 200 μL. Therefore, crystals were formed on the PDMS substrate through slow evaporation under ambient temperature. The DA/PDMS films were then characterized without any additional poling treatment.

4.5 | Optical Microscopy

An examination on the surface features of DA crystalline and DA/SF films was carried out using a stereoscopic optical microscope (SteREODiscovery V20, Zeiss, Germany).

4.6 | Scanning Electron Microscopy (SEM)

The scanning electron microscopy (SEM; JSM-IT500LA, JEOL, Japan) was used to carry out examination of the microstructural characteristics of these samples; therefore, analyses were conducted on both their surface and cross sectional regions. Hence, energy-dispersive x-ray spectroscopy (EDS) was additionally employed to make evaluation of the spatial distribution situation of chlorine elements inside the selected areas.

4.7 | Mechanical Property

The mechanical performance of these films was measured through a universal testing system Instron 5967, USA. Before the testing activity is carried out, all test samples were cut into rectangle-shaped strips with size of 1 cm × 4 cm × 0.05 mm. Uniaxial tensile measurement work was performed with crosshead

speed set as 1 mm min^{-1} for acquiring stress–strain curves. Therefore, based on these curve graphs, key mechanical parameters containing Young's modulus, elongation at break, and tensile strength were calculated in the subsequent process hence.

4.8 | Fourier-Transform Infrared Spectroscopy (FTIR)

Fourier transform infrared spectroscopy (FTIR; NEXUS 670, Thermo Nicolet, USA) was employed to analyze the secondary structural features of the SF films. Spectral data in the range of 400–4000 cm^{-1} were collected. The resolution was 2 cm^{-1} and 64 scans were accumulated for each sample. Subsequent deconvolution and assignment of protein secondary structures were performed according to previously reported methodologies [31]. For differential FTIR analysis, the PSF spectrum was subtracted from the spectra of 1DSF, 2DSF, 3DSF, and 4DSF to obtain the corresponding difference spectra, which were used to assess DA-induced changes in SF molecular interactions and structure.

4.9 | X-Ray Diffraction (XRD)

The structural crystallinity of the samples was analyzed via x-ray diffraction (XRD) using a Bruker D8 ADVANCE instrument (Germany), which was fitted with a Cu-Kα radiation source and operated under conditions of 40 kV voltage and 60 mA current. The XRD scans for the SF films were collected across a 2θ angular range from 5° to 45°, employing a step size of 0.03° and a dwell time of 3 s at each step. The degree of crystallinity was quantified through analysis of the acquired diffraction profiles using the reported methodologies. Additionally, the crystalline properties of the SF films were further evaluated using wide-angle x-ray scattering (WAXS). For the examination of single crystals, DA crystals cultivated on PDMS films were first observed under a polarized optical microscope (Zeiss Ci-POL, Germany) to confirm their crystallinity before undergoing XRD analysis. Single-crystal diffraction data were processed using APEX5 software to determine the crystallographic parameters. The resulting crystallographic information files (CIFs) were submitted to the IUCr CheckCIF platform for structural validation (Note S4).

4.10 | Transmittance

The optical transmittance of the films was characterized using ultraviolet–visible spectroscopy (Lambda 950, PerkinElmer, USA).

4.11 | Ferroelectric Measurement

To investigate the ferroelectric behavior of SF films, disc-shaped samples with a diameter of 6 mm were fabricated. Gold electrodes measuring 2 mm in diameter were sputtered onto both sides of each disc. A ferroelectric measurement instrument (FEAI1000, Balab Technologies, China) was used to obtain the polarization–electric field (P–E) hysteresis loops.

4.12 | Relative Permittivity Measurement

The relative permittivity and dielectric loss of the DA/SF films as a function of frequency was measured using a precision LCR meter (WKSMD/WK6500, Balab Technologies, China) over a broad frequency range.

4.13 | Piezoelectric Coefficient (D33) Characterization

A quasi-static d_{33} meter (PEAI1000, Balab Technologies, China) was employed to evaluate the piezoelectric d_{33} coefficient. Measurements were performed under a static load of 3 N together with a dynamic load of 0.25 N. To ensure statistical validity, 5–6 randomly selected regions were measured for each film sample. To evaluate the thermal stability of the films, the d_{33} was measured using a temperature-controlled piezoelectric testing system (PEMS6000LN, Balab Technologies, China). The measurements were performed from 20°C to 100°C at 10°C intervals.

4.14 | Piezoelectric Force Microscopy (PFM)

To further investigate the microscopic ferroelectric and piezoelectric characteristics, PFM detections were performed on the DA/SF films using a Jupiter XR instrument (Oxford Instruments, UK). All measurements were performed using a conductive Pt-coated probe (ContE-G, Budget Sensors, Bulgaria), with both the cantilever and tip metallized for enhanced electrical contact. For each measurement site, a $5 \times 5\ \mu m^2$ region was examined in DART mode with an applied drive voltage of 5 V. In addition, single-point SS-PFM hysteresis loops were obtained using a trigger voltage of 20 V.

4.15 | Preparation of Mechanical Sensors Based on DA/SF Films

Figure 4A illustrates the fabrication process of the force sensor based on DA/SF films. Briefly, two 2DSF films were electrically connected in series using Mo electrodes deposited by silver pasting. Meanwhile, the PDMS film with a single-sided Mo electrode was prepared and employed to encapsulate the piezoelectric DA/SF films. The device was subsequently connected to an oscilloscope (UNI-T UPO1202S-E, China) via leads to record the voltage waveforms generated in response to applied mechanical stimuli.

4.16 | Voltage Output Measurement

All procedures involving human volunteers were conducted in compliance with relevant ethical standards and regulations, with approval granted by the Ethics Committee of the Affiliated Stomatology Hospital of Chongqing Medical University (approval no. CQHS-REC-2023 (LS no. 054)). Written informed consent was obtained from each participant prior to the study. Initially, a calibrated stepper motor applied controlled force at a set frequency to the force sensors to record the resulting voltage waveforms. Subsequently, to evaluate performance in biological

settings, the sensors were attached to temporomandibular joints. Voltage waveforms produced by joint motions were recorded at various kinds of movements: the open and close movements, the lateral-left and lateral-right movements, the protrusion and retrusion movements. Furthermore, the devices were positioned on the occlusal surfaces of various teeth to detect voltage signals generated under different occlusal contact patterns. Specifically, the voltage waveforms generated at premolar and molar regions during the lateral movements were recorded, as well as those produced at anterior teeth during the protrusion movements.

4.17 | Density Functional Theory (DFT) Calculations

A representative polar-stacking of antiparallel β-sheet that commonly observed in SF was selected as the model system [26]. In addition, a 3D molecular model was constructed comprising two antiparallel polypeptide chains with repeating sequences (GAGAGA and AGAGAG). Given that such an arrangement may undergo relative displacement under external mechanical force, several structural models were further developed to simulate potential deformation modes induced by mechanical stress, including the original antiparallel configuration, a "close approach" stacking mode, and two displacement types (designated as register shift 1 and register shift 2). DFT calculations were then performed to determine key electronic properties for each model, including the charge density distribution, contour plots of charge density and dipole moment. Detailed computational procedures are presented in Note S5.

4.18 | Biocompatibility Assessment In Vitro

All animal- and cell-related experiments in this work were approved by the Ethics Committee of the Affiliated Stomatology Hospital of Chongqing Medical University (approval no. CQHS-REC-2023 (LS no. 054)). To evaluate the biocompatibility of SF and DA/SF samples, rat bone marrow–derived mesenchymal stem cells (BMSCs) were incubated with media containing extracts of the two materials (10 μg/mL).

Cell proliferation of BMSCs was evaluated on Days 1 and 3 using the CCK-8 assay. At the indicated time points, the tests were conducted in accordance with the manufacturer's protocol. All experimental groups were run in five replicates. Cell viability was evaluated by employing a live/dead staining protocol following one day of BMSCs culture. Fluorescence imaging was performed using a Zeiss Axio Obserber7 microscope (Germany). Excitation at 488 nm (for live cells) and 560 nm (for dead cells) was applied, and five randomly selected fields of view per well were captured for analysis.

To examine cell morphology and cytoskeletal structure, actin filaments and nuclei were fluorescently stained after 1 day of culture. F-actin was labeled by co-culture with rhodamine-conjugated phalloidin for 30 min, while nuclei were counterstained with DAPI for 15 min. Fluorescence images were acquired by using excitation wavelengths of 408 nm for DAPI and 488 nm for phalloidin.

4.19 | Biocompatibility Assessment In Vivo

To carry out assessment for in vivo biocompatibility of SF and DA/SF films, 8-week-old male Sprague-Dawley rats were obtained from Animal Center of Chongqing Medical University. Therefore, all animals were kept in a pathogen-free, controlled environment during the whole study process. For surgical implantation activity, anesthesia was first started by way of inhalation of 2%–5% isoflurane, and hence maintained at 2% concentration. After anesthesia was achieved, a longitudinal cut was made along the back, and then SF and DA/SF films were inserted into subcutaneous area. Thus, the incision was closed by using sutures. Blood samples were taken on the third, fifth, and seventh days after surgery for later analysis. Animals were euthanized at 7 and 14 days after implantation. At each preset time point, tissue samples around the implant site, as well as important organs including heart, liver, spleen, lungs, and kidneys, were collected and treated for histopathological examination, in order to monitor local inflammatory responses and possible systemic toxic effects.

4.20 | Statistical Analysis

All experiments were carried out in three repeated times. Before we do statistical analysis, we first assess data for normality and variance homogeneity, hence one-way analysis of variance (ANOVA) was used for comparisons among multiple groups, thus followed by Tukey's test for post hoc pairwise analysis. Data are shown as mean ± standard deviation (SD). Therefore, data were statistically analyzed with SPSS software (version 24.0), and we define statistical significance as a p value smaller than 0.05.

Acknowledgements

The authors express deep gratefulness to the Roentgen Laboratory for providing supporting help with XRD and WAXS measurements. Besides, computational assistance related to DFT calculations was supplied by Shenzhen Huasuan Technology Co., Ltd.

Funding

This research received financial support from the National Natural Science Foundation of China (U22A20314 and 82401124), China Postdoctoral Science Foundation (2025M771772), Chongqing Post-doctoral Science Special Foundation (2024CQBSHTB3111), and the Postdoctoral Fellowship Program (Grade C) of China Postdoctoral Science Foundation (GZC20251227).

Conflicts of Interest

The authors declare no conflicts of interest.

Data Availability Statement

The data that support the findings of this study are available from the corresponding author upon reasonable request.

References

1. F. Li, B. O. Wang, X. Gao, D. Damjanovic, L. Q. Chen, and S. Zhang, "Ferroelectric Materials Toward Next-Generation Electromechanical Technologies," *Science* 389 (2025): adn4926.

2. Z. Hui, L. Zhang, G. Ren, G. Sun, H. D. Yu, and W. Huang, "Green Flexible Electronics: Natural Materials, Fabrication, and Applications," *Advanced Materials* 35 (2023): 2211202.

3. Z. Zhang, Z. Wang, X. Li, Y. I. Zheng, and Z. Yang, "Design and Manufacturing of Piezoelectric Biomaterials for Bioelectronics and Biomedical Applications," *Chemical Reviews* 125 (2025): 9875–9929.

4. D. Kim, S. A. Han, J. H. Kim, et al., "Biomolecular Piezoelectric Materials: From Amino Acids to Living Tissues," *Advanced Materials* 32 (2020): 1906989.

5. S. Guerin, A. Stapleton, and D. Chovan, "Control of Piezoelectricity in Amino Acids by Supramolecular Packing," *Nature Materials* 17 (2018): 180–186.

6. Y. Cheng, T. Wang, and H. Zhu, "Molecular Engineering of Amino Acid Crystals With Enhanced Piezoelectric Performance for Biodegradable Sensors," *Angewandte Chemie International Edition* 64 (2025): 202500334.

7. H. Wu, H. Lyu, H. Jiang, et al., "Bioinspired Supramolecular Fibrillization Enables Stretchable and Biodegradable Piezoelectric Bioelectronics," *Science Advance* 11 (2025): adu6759.

8. F. Yang, J. Li, and Y. Long, "Wafer-Scale Heterostructured Piezoelectric Bio-Organic Thin Films," *Science* 373 (2021): 337–342.

9. J. Chen, C. Zhang, R. Liu, et al., "Visible Periodic Piezoelectric Domains in Silk Fibroin for Neurite-Orientated Extension," *Advanced Materials* 37 (2025): 2415053.

10. H. Y. Zhang, Y. Y. Tang, and Z. X. Gu, "Biodegradable Ferroelectric Molecular Crystal With Large Piezoelectric Response," *Science* 383 (2024): 1492–1498.

11. Q. Niu, J. Chen, and S. Fan, "Silk Nanoribbon Films with Enriched Silk II Structure and Enhanced Piezoelectricity for Self-Powered Implantable and Wearable Devices," *Nano Today* 56 (2024): 102228.

12. H. A. Tran, T. T. Hoang, and A. Maraldo, "Emerging Silk Fibroin Materials and Their Applications: New Functionality Arising From Innovations in Silk Crosslinking," *Materials Today* 65 (2023): 244–259.

13. H. Ding, D. Chen, and X. Tan, "Enhanced Bone Repair Using Callus Organoids Derived From Urine-Derived Stem Cells With Silk Fibroin," *Advanced Healthcare Materials* 14 (2025): 2501852.

14. V. Sencadas, C. Garvey, S. Mudie, J. J. K. Kirkensgaard, G. Gouadec, and S. Hauser, "Electroactive Properties of Electrospun Silk Fibroin for Energy Harvesting Applications," *Nano Energy* 66 (2019): 104106.

15. X. Wang, W. Fan, and Y. Liu, "Bioadhesive and Conformable Bioelectronic Interfaces for Vasomotoricity Monitoring and Regulation," *Nature Communications* 16 (2025): 9103.

16. S. Yang, C. Zhao, Y. Yang, J. Ren, and S. Ling, "The Fractal Network Structure of Silk Fibroin Molecules and Its Effect on Spinning of Silkworm Silk," *ACS Nano* 17 (2023): 7662–7673.

17. Y. Wang, X. Feng, and X. Chen, "Autonomous Bioelectronic Devices Based on Silk Fibroin," *Advanced Materials* 37 (2025): 2500073.

18. B. Zhu, H. Wang, and W. R. U. Leow, "Silk Fibroin for Flexible Electronic Devices," *Advanced Materials* 28 (2016): 4250–4265.

19. C. Zhang, Y. Zhou, H. Han, H. Zheng, W. Xu, and Z. Wang, "Dopamine-Triggered Hydrogels With High Transparency, Self-Adhesion, and Thermoresponse as Skinlike Sensors," *ACS Nano* 15 (2021): 1785–1794.

20. Y. Zhu, M. Lu, F. Gao, C. Zhou, C. Jia, and J. Wang, "Role of Tailor-Made Additives in Crystallization From Solution: A Review," *Industrial & Engineering Chemistry Research* 62 (2023): 4800–4816.

21. H. Hemmatpour, O. De Luca, and D. Crestani, "New Insights in Polydopamine Formation via Surface Adsorption," *Nature Communications* 14 (2023): 664.

22. L. Wang and J. Liu, "Dopamine Polymerization-Mediated Surface Functionalization Toward Advanced Bacterial Therapeutics," *Accounts of Chemical Research* 57 (2024): 945–956.

23. G. S. Lee, T. Yun, and H. Kim, "Mussel Inspired Highly Aligned $Ti_3C_2T_X$ MXene Film With Synergistic Enhancement of Mechanical Strength and Ambient Stability," *ACS Nano* 14 (2020): 11722–11732.

24. X. Tan, H. E. Wang, and K. Wang, "One-Step Construction of Biocompatible Glycine Assemblies With Exceptional Piezoelectric Performance for Sustainable Electronics," *Advanced Functional Materials* 35 (2025): 2506107.

25. L. Zhou, J. Justin Koh, and X. Hou, "The Crystallization of Decanoic Acid/Dopamine Supramolecular Self-Assemblies in the Presence of Coacervates," *Journal of Colloid and Interface Science* 615 (2022): 759–767.

26. L. D. Koh, Y. Cheng, and C. P. Teng, "Structures, Mechanical Properties and Applications of Silk Fibroin Materials," *Progress in Polymer Science* 46 (2015): 86–110.

27. L. Fan, Z. Cai, and J. Zhao, "Gelation Dynamics, Formation Mechanism, Functionalization, and 3D Bioprinting of Silk Fibroin Hydrogel Materials for Biomedical Applications," *ACS Nano* 19 (2025): 17979–18002.

28. T. Yucel, P. Cebe, and D. L. Kaplan, "Structural Origins of Silk Piezoelectricity," *Advanced Functional Materials* 21 (2011): 779–785.

29. D. N. Rockwood, R. C. Preda, T. Yücel, X. Wang, M. L. Lovett, and D. L. Kaplan, "Materials Fabrication From Bombyx Mori Silk Fibroin," *Nature Protocols* 6 (2011): 1612–1631.

30. L. Jin, Y. Tai, and J. Nam, "Piezoelectric Silk Fibroin Nanofibers: Structural Optimization to Enhance Piezoelectricity and Biostability for Neural Tissue Engineering," *Nano Energy* 132 (2024): 110367.

31. D. Eliaz, S. Paul, and D. Benyamin, "Micro and Nano-Scale Compartments Guide the Structural Transition of Silk Protein Monomers Into Silk Fibers," *Nature Communications* 13 (2022): 7856.

32. N. Drnovsek, R. Kocen, and A. Gantar, "Size of Silk Fibroin β-Sheet Domains Affected by Ca^{2+}," *Journal of Materials Chemistry B* 4 (2016): 6597–6608.

33. K. Yazawa, K. Ishida, H. Masunaga, T. Hikima, and K. Numata, "Influence of Water Content on the β-Sheet Formation, Thermal Stability, Water Removal, and Mechanical Properties of Silk Materials," *Biomacromolecules* 17 (2016): 1057–1066.

34. D. Wen, H. Wang, X. Zhu, et al., "Conformation and Crystallinity of Silk Fibroin," *Journal of Textile Research* 26 (2005): 110–112.

35. J. Chen, Z. Pei, and B. Chai, "Engineering the Dielectric Constants of Polymers: from Molecular to Mesoscopic Scales," *Advanced Materials* 36 (2024): 2308670.

36. B. Jiang, J. Iocozzia, and L. Zhao, "Barium Titanate at the Nanoscale: Controlled Synthesis and Dielectric and Ferroelectric Properties," *Chemical Society Reviews* 48 (2019): 1194–1228.

37. H. Xue, J. Jin, and Z. Tan, "Flexible, Biodegradable Ultrasonic Wireless Electrotherapy Device Based on Highly Self-Aligned Piezoelectric Biofilms," *Science Advances* 10 (2024): adn0260.

38. J. Li, C. Carlos, and H. Zhou, "Stretchable Piezoelectric Biocrystal Thin Films," *Nature Communications* 14 (2023): 6562.

39. Q. Lv, S. Chen, and D. Luo, "An Implantable and Degradable Silk Sericin Protein Film Energy Harvester for Next-Generation Cardiovascular Electronic Devices," *Advanced Materials* 37 (2025): 2413610.

40. C. M. Longman and G. J. Pearson, "Variations in Tooth, Surface Temperature in the Oral Cavity during Fluid Intake," *Biomaterials* 8 (1987): 411–414.

41. C. W. Barclay, D. Spence, and W. R. E. Laird, "Intra-Oral Temperatures During Function," *Journal of Oral Rehabilitation* 32 (2005): 886–894.

42. A. Gruverman, M. Alexe, and D. Meier, "Piezoresponse Force Microscopy and Nanoferroic Phenomena," *Nature Communications* 10 (2019): 1661.

43. P. Buragohain, H. Lu, and C. Richter, "Quantification of the Electromechanical Measurements by Piezoresponse Force Microscopy," *Advanced Materials* 34 (2022): 2206237.

44. J. Kwon and H. Cho, "Piezoelectric Heterogeneity in Collagen Type I Fibrils Quantitatively Characterized by Piezoresponse Force Microscopy," *ACS Biomaterials Science & Engineering* 6 (2020): 6680–6689.

45. R. E. Marsh, R. B. Corey, and L. Pauling, "An Investigation of the Structure of Silk Fibroin," *Biochimica et Biophysica Acta* 16 (1955): 1–34.

46. E. Fukada, "Piezoelectric Properties of Biological Polymers," *Quarterly Reviews of Biophysics* 16 (1983): 59–87.

47. G. Das Adhikary, A. Adukkadan, and G. J. Muleta, "Longitudinal Strain Enhancement and Bending Deformations in Piezoceramics," *Nature* 637 (2025): 333–338.

48. Y. García, Y. B. Ruiz-Blanco, Y. Marrero-Ponce, et al., "Orthotropic Piezoelectricity in 2D Nanocellulose," *Scientific Reports* 6 (2016): 34616.

49. D. Denning, J. I. Kilpatrick, and E. Fukada, "Piezoelectric Tensor of Collagen Fibrils Determined at the Nanoscale," *ACS Biomaterials Science & Engineering* 3 (2017): 929–935.

50. B. Y. Lee, J. Zhang, and C. Zueger, "Virus-Based Piezoelectric Energy Generation," *Nature Nanotechnology* 7 (2012): 351–356.

51. M. Ha, B. Choi, S. H. Joo, et al., "Biodegradable, Electro-Active Chitin Nanofiber Films for Flexible Piezoelectric Transducers," *Nano Energy* 48 (2018): 275–283.

52. J. H. Kim, M. Lee, C. B. Park, et al., "Polydopamine as a Biomimetic Electron Gate for Artificial Photosynthesis," *Angewandte Chemie* 53 (2014): 6364–6368.

53. The Glossary of Prosthodontic Terms 2023, *The Journal of Prosthetic Dentistry* 130 (2023): e7–e126.

54. H. Feng, W. Song, and R. Li, "A Fully Integrated Orthodontic Aligner With Force Sensing Ability for Machine Learning-Assisted Diagnosis," *Advanced Science* 12 (2025): 2411187.

55. Y. Yan, L. Yu, and X. Zhang, "Instantaneous Self-Recovery and Ultra-Low Detection Limit Hydrogel Electronic Sensor for Temporomandibular Disorders Intelligent Diagnosis," *Nature Communications* 16 (2025): 839.

56. E. Mancuso, A. Forte, and T. Maravic, "Effects of Preparation Design on the Marginal and Internal Fit of CAD-CAM Overlay Restorations: A μCT Evaluation," *The Journal of Prosthetic Dentistry* 133 (2025): 1055.e1.

57. S. Gismondi, G. Ruggiero, R. Bollero, F. Enrico, F. Zarone, and R. Sorrentino, "A Digital Technique for Fabricating a Diagnostic Occlusal Device Using Mandibular Motion Tracking," *Digital Dentistry Journal* 1 (2025): 100012.

58. H. Ma, B. Shao, T. Zheng, and Z. Liu, "Differentiating Temporomandibular Disorder Subtypes Using Advanced Kinematic Parameters: A Novel Approach to the Diagnosis of Temporomandibular Disorders," *Journal of Biomechanics* 189 (2025): 112849.

59. B. Shao, H. Teng, S. Dong, and Z. Liu, "Finite Element Contact Stress Analysis of the Temporomandibular Joints of Patients with Temporomandibular Disorders Under Mastication," *Computer Methods and Programs in Biomedicine* 213 (2022): 106526.

60. Y. Du, J. Song, H. Liu, et al., "Self-powered Triboelectric Sensor for Real-Time, Intelligent Occlusal Force Monitoring," *Advanced Functional Materials* 36 (2025): 19646.

61. R. Lin, Y. Fan, and Y. Xie, "A Self-Powered Wearable Seizure-Monitoring/Brain-Stimulating System for Potential Epilepsy Treatment," *Nano Energy* 107 (2023): 108121.

62. T. Zhong, M. Zhang, and Y. Fu, "An Artificial Triboelectricity-Brain-Behavior Closed Loop for Intelligent Olfactory Substitution," *Nano Energy* 63 (2019): 103884.

63. Q. Niu, H. Wei, B. S. Hsiao, and Y. Zhang, "Biodegradable Silk Fibroin-Based Bio-Piezoelectric/Triboelectric Nanogenerators as Self-Powered Electronic Devices," *Nano Energy* 96 (2022): 107101.

64. J. K. Sahoo, O. Hasturk, T. Falcucci, and D. L. Kaplan, "Silk Chemistry and Biomedical Material Designs," *Nature Reviews Chemistry* 7 (2023): 302–318.

65. Z. Xu, M. Wu, W. Gao, and H. Bai, "A Sustainable Single-Component "Silk Nacre"," *Science Advances* 8 (2022): abo0946.

66. H. Lee, S. M. Dellatore, W. M. Miller, and P. B. Messersmith, "Mussel-Inspired Surface Chemistry for Multifunctional Coatings," *Science* 318 (2007): 426–430.

67. J. H. Waite, "Mussel Power," *Nature Materials* 7 (2008): 8–9.

68. Y. Liu, S. Yang, Q. Wang, et al., "Biomimetic Hierarchical Molecular Assembly of Silk-Hydroxyapatite Composites for Near-Native Bone Regeneration," *Advanced Functional Materials* 36 (2025): 24279.

Supporting Information

Additional supporting information can be found online in the Supporting Information section.

Supporting File: adma74240-sup-0001-SuppMat.pdf.